Chapter 12
Fluid-structure Interaction with Contact

Guest Article by Stefan Frei
University College London
s.frei@ucl.ac.uk

Based on the dissertation
Eulerian finite element methods for interface problems and fluid-structure interactions.
Universität Heidelberg 2016 [151].

In this chapter, we revisit the problem of an elastic ball falling down towards the ground by gravity within a viscous fluid, that was already briefly discussed in Sect. 6.6.3. To deal with the topology change at contact time, we use a *Fully Eulerian approach* as introduced in Sect. 3.6 and detailed in Chap. 6.

An accurate study of the contact dynamics requires discretization techniques in space and time that take into account the interface movement. Here, we will use the *locally modified finite element* technique introduced in Sect. 4.5 for accurate space discretization and the modified Galerkin approach as described in Sect. 4.6 for time discretization.

We will be especially interested in the question of whether it comes to contact between ball and ground, or whether a thin fluid layer remains in between them. From the point of view of analysis, this is an open problem if the ball is considered elastic, cf. Remark 6.13. Physical experiments indicate that it comes to real contact in many situations, consider e.g. the fall of a steel ball towards the ground within air. In this case, some of the assumptions made in the derivation of the incompressible Navier-Stokes equations will not be valid anymore (e.g. the continuum assumption, a linear stress-strain-relationship and incompressibility). Due to the lack of a validated model for the fluid for the case of contact, however, we stick here to the incompressible Navier-Stokes equations, expecting that the small time slot around the contact interval, where they are not an appropriate model, does not influence the dynamics too much.

If it comes to contact, we have to deal with variational inequalities. Here, we use a simple contact algorithm based on a penalty formulation, motivated by a work of Sathe and Tezduyar [298].

T. Richter, *Fluid-structure Interactions*, Lecture Notes in Computational Science and Engineering 118, DOI 10.1007/978-3-319-63970-3_12

12.1 Problem Setting and Equations

We begin with a simple model problem, see Fig. 12.1, where an elastic ball falls down towards the planar ground $\Gamma_w = \{(x, y) \in \mathbb{R}^2 \,|\, y = -1\}$ by a gravity force. We consider a ball of radius $r = 0.4$ whose midpoint is initially located at the origin. As boundary condition, we impose a homogeneous velocity on Γ_w. In combination with the *kinematic condition* and the velocity—displacement relation $d_t \mathbf{u}_s = \mathbf{v}_s$ this ensures that the ball cannot pass "through the ground". We assume that the simulation domain $\Omega = (-1, 1) \times (-1, 0.5)$ is open on the lateral and upper boundaries and use the *do-nothing* outflow condition there.

The corresponding variational formulation in fully Eulerian coordinates reads (cf. Problem (6.6)):

Find the global velocity $\mathbf{v} \in \mathbf{v}^D + \mathcal{V}$, *the solid displacement* $\mathbf{u}_s \in \mathbf{u}_s^D + \mathcal{W}_s$, *and the fluid pressure* $p_f \in \mathcal{L}_f$ *such that*

$$\begin{aligned} &(\rho(\partial_t \mathbf{v} + \mathbf{v} \cdot \nabla \mathbf{v}), \phi)_\Omega \\ &\quad + (\boldsymbol{\sigma}, \nabla \phi)_\Omega - \langle \rho_f \nu_f \nabla \mathbf{v}^T \mathbf{n}_f, \phi \rangle_{\Gamma_f \setminus \Gamma_f^d} = (\rho \mathbf{f}, \phi)_\Omega \quad \forall \phi \in \mathcal{V}, \\ &\quad (\partial_t \mathbf{u}_s + \mathbf{v} \cdot \nabla \mathbf{u}_s - \mathbf{v}, \psi_s)_{\mathcal{S}(t)} = 0 \quad \forall \psi_s \in \mathcal{W}_s, \\ &\quad (\operatorname{div} \mathbf{v}, \xi_f)_{\mathcal{F}(t)} = 0 \quad \forall \xi_f \in \mathcal{L}_f. \end{aligned} \tag{12.1}$$

Here we have used the abbreviations $\rho|_{\mathcal{S}} = \rho_s = J \rho_s^0$ and $\rho|_{\mathcal{F}} = \rho_f$. Furthermore, we have defined $\boldsymbol{\sigma}|_{\mathcal{F}} = \boldsymbol{\sigma}_f$ and $\boldsymbol{\sigma}|_{\mathcal{S}} = \boldsymbol{\sigma}_s$ and analogously for the right-hand side $\mathbf{f}$. The function spaces are given by

$$\mathcal{V} = H_0^1(\Omega; \Gamma_f^d \cup \Gamma_s^d)^2, \quad \mathcal{W}_s := H_0^1(\mathcal{S}(t); \Gamma_s^d)^2, \quad \mathcal{L}_f := L^2(\mathcal{F}(t)).$$

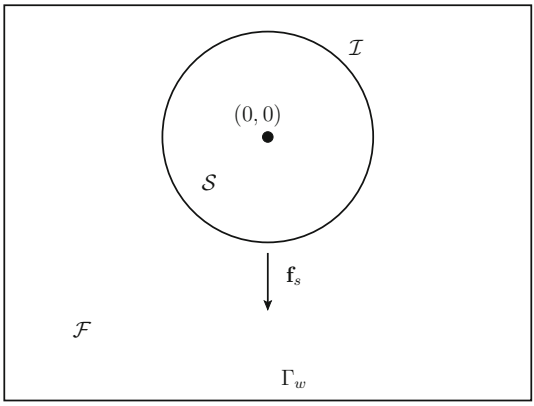

Fig. 12.1 Sketch of the configuration of the first test case

The fluid boundary term on the left-hand side stems from the fact that the full symmetric stress tensor

$$\boldsymbol{\sigma}_f = \rho_f \nu_f (\nabla \mathbf{v} + \nabla \mathbf{v}^T) - p_f I$$

enters the fluid equations, while the *do-nothing* condition on $\Gamma_f \setminus \Gamma_f^d$ includes the reduced stress tensor $\boldsymbol{\sigma}_f^{\text{red}} = \rho_f \nu_f \nabla \mathbf{v}_f - p_f I$. For the solid, we use a St.Venant Kirchhoff material law

$$\boldsymbol{\sigma}_s = J_s \mathbf{F}_s^{-1} \left(2\mu_s \mathbf{E}_s + \lambda_s \text{tr}(\mathbf{E}_s)\right) \mathbf{F}_s^{-T}. \tag{12.2}$$

with the Green-Lagrange strain $\mathbf{E}_s = \frac{1}{2}(\mathbf{F}_s^{-T}\mathbf{F}_s^{-1} - I)$.

To capture the moving interface, we use the initial point set method, as described in Sect. 6.2. The system is supplemented with the initial conditions

$$\mathbf{v}(x,0) = \mathbf{v}^0(x) \quad \text{in } \Omega, \qquad \mathbf{u}(x,0) = \mathbf{u}^0(x) \quad \text{in } \mathcal{S}(0).$$

12.2 Space Discretization and Pressure Stabilization

For spatial discretization, we use *equal-order* locally modified finite elements (cf. Sect. 4.5) for all the components of the solution. For ease of implementation, we use the global space $\mathcal{V}_h$ on the whole domain Ω for all the variables and use artificial extensions of the fluid pressure p_f and the solid displacement $\mathbf{u}_s$ to the complete domain Ω.

This choice for velocity and pressure violates the *inf-sup* condition in the fluid problem that is necessary to ensure the well-posedness of the discrete system of equations, cf. Sect. 4.3.2. To cope with this, we will add stabilization terms to the discrete variational formulation.

The challenge for pressure stabilization within the *locally modified finite element method* lies in the anisotropies that are present in the interface region including abrupt changes of anisotropy between neighboring cells, see Fig. 12.2 for an example. Typically, the stabilization methods used on anisotropic meshes require an assumption on the change of anisotropy between neighboring cells that can not be guaranteed here (see e.g. Braack and Richter [62]).

To deal with this, we will use a variant of the *Continuous Interior Penalty* (CIP) stabilization technique introduced by Burman and Hansbo [84–86]. We denote the set of cells of the fluid domain by Ω_h^f and the set of edges by $\mathcal{E}_h$. The original CIP technique is based on penalizing jumps of the gradient over element edges

$$S(p_h, \xi_h) := \gamma h^s \sum_{e \in \mathcal{E}_h} \int_e [\nabla p_h]_e \cdot [\nabla \xi_h]_e \, do,$$

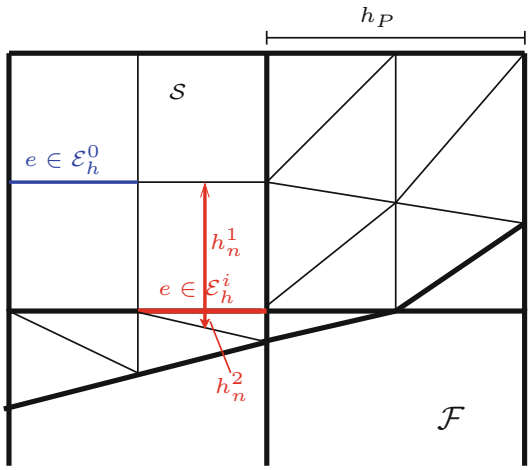

Fig. 12.2 Sketch of four patches in the interface region. The cell sizes in normal direction h_n^1 and h_n^2 for $e \in \mathcal{E}_h^i$ vary significantly

with $s = 2$ or $s = 3$. This does not guarantee stability in the case of abrupt changes of anisotropy, however, as the cell sizes of the two neighboring cells in direction normal to the edge can be very different. Hence, we have to modify this technique in the interface patches. Here, we will use a weighted average of the pressure gradient instead of the jump terms.

To define a variant suitable for anisotropic meshes, we split the set of edges into two parts: By $\mathcal{E}_h^0$, we denote all edges that lie between two quadrilateral cells $K_1, K_2 \subset \Omega_h^f$. By $\mathcal{E}_h^i$ we denote the edges that are edges of at least one triangular element $K \subset \Omega_h^f$, see Fig. 12.2. In other words, this means that $\mathcal{E}_h^i$ contains all edges that are part of patches cut by the interface.

We define the stabilization term by

$$S_{\text{aniso}}(p_h, \xi_h) := \gamma h_P^2 \sum_{e \in \mathcal{E}_h^i} \int_e \{h_n \nabla p_h \cdot \nabla \xi_h\}_e \, \mathrm{d}o + \gamma h_P^2 \sum_{e \in \mathcal{E}_h^0} \int_e h_n [\nabla p_h]_e \cdot [\nabla \xi_h]_e \, \mathrm{d}o,$$

where $\gamma > 0$ is a constant, h_P is the size of the patch, h_n is the cell size in the direction normal to e, $[\cdot]_e$ denotes the jump term across the edge e and

$$\{\mathbf{v}_h\}_e := \frac{1}{2} \left(\mathbf{v}_{h|K_1} + \mathbf{v}_{h|K_2} \right)$$

is the mean value of the two cells K_1, K_2 sharing the edge e. In the case that one of the cells K_1, K_2 does not lie in Ω_h^f, we set the respective contribution to zero. This term is then added to the divergence equation

$$(\text{div } \mathbf{v}_h, \xi_h)_{\mathcal{F}(t)} + S_{\text{aniso}}(p_h, \xi_h) = 0 \quad \forall \xi_h \in \mathcal{V}_h^f.$$

In contrast to the original CIP technique this stabilization is not consistent anymore, in the sense that the continuous solution fulfills the discrete, stabilized system. However, it can been shown [151] that the inconsistency is sufficiently small, such that the stabilized, discrete solution is of second-order, as is the discretization error of the *locally modified finite element* scheme of order one.

12.3 Time Discretization

For time discretization, we use the dG(0) variant of the modified time stepping scheme presented in Sect. 4.6. In this section, we will give practical details on how to compute a suitable mapping $T_m : \Omega_m \times I_m \to Q^m$ for a time interval $m = 1, \ldots, M$.

To simplify the implementation, we use the old deformation u^{m-1} to define the subdomains $\mathcal{F}^m$ and $\mathcal{S}^m$ and the interface $\mathcal{I}^m$ explicitly. Note that a fully implicit integration of the domain affiliation within a Newton-type algorithm would require the calculation of shape derivatives, compare Sect. 6.4.

Then, we use the new domain Ω^m as reference domain for the time interval $I_m = [t_{m-1}, t_m]$ and define a map $T_m : \Omega_m \times I_m \to Q^m$ which is linear in time. We define

$$T_m(x,t) = \frac{t_m - t}{t_m - t_{m-1}} T_m(x, t_{m-1}) + \frac{t - t_{m-1}}{t_m - t_{m-1}} x. \tag{12.3}$$

This implies in particular $T_m(x, t_m) = x$. It remains to specify the mapping T_m at time t_{m-1} in such a way that points x lying on the interface $\mathcal{I}(t_m)$ at time t_m are mapped to points on the interface $\mathcal{I}(t_{m-1})$ at time t_{m-1}. We have already seen in the numerical example in Sect. 4.6 that this requirement is fulfilled by the function

$$\tilde{T}_m(t_{m-1}) = (\Psi_{\text{IPS}}(t_{m-1}))^{-1} \circ \Psi_{\text{IPS}}(t_m)$$

where $\Psi_{\text{IPS}}(t_k)$ denotes the *Initial Point Set* function at time t_k that has been introduced in Sect. 6.2. In practice, we calculate $x^{m-1} := \tilde{T}_m(x^m, t_{m-1})$ in a point $x^m \in \Omega^m$ by applying Newton's method to

$$\Psi_{\text{IPS}}(t_{m-1})(x^{m-1}) = \Psi_{\text{IPS}}(t_m)(x^m),$$

i.e.

$$x^{m-1} - u^{m-2}(x^{m-1}) = x^m - u^{m-1}(x^m). \tag{12.4}$$

It is sufficient to use this mapping $\tilde{T}_m$ in the interface region. Far away from the interface, we define T_m as the identity. In between, we define a smooth transition by using a function g depending on the distance to the interface with $g = 1$ in a point $x \in \Omega^{m-1}$ with $\mathrm{dist}_{\mathcal{I}(t_{m-1})}(x) < \varepsilon$ and $g = 0$ if $\mathrm{dist}_{\mathcal{I}(t_{m-1})}(x) > \delta$ for $\delta > \varepsilon > 0$. We set

$$T_m(t,x) = g(x)\tilde{T}_m(t,x) + (1 - g(x))\,\mathrm{id}.$$

The modified $dG(0)$ time stepping scheme for the fluid-structure interaction problem (12.1) reads: *Find* $\mathbf{v} \in (\mathbf{v}^D + \mathcal{V}^m)$, $\mathbf{u}_s \in (\mathbf{u}_s^D + \mathcal{W}_s^m)$, *and* $p_f \in \mathcal{L}_f^m$ *such that*

$$\begin{aligned}(\rho(\mathbf{v}^m - \mathbf{v}^{m-1}), \phi)_{\Omega^m} + k(\rho(\mathbf{v}^m - \partial_t T_m)\nabla\mathbf{v}^m, \phi)_{\Omega^m} + k(\boldsymbol{\sigma}, \nabla\phi)_{\Omega^m} \\ -k\langle \rho_f \nu_f \nabla^T \mathbf{v}_f^m \mathbf{n}, \phi\rangle_{\Gamma_f \setminus \Gamma_f^D} = k(\mathbf{f}^m, \phi)_{\Omega^m},\\ (\mathbf{u}^m - \mathbf{u}^{m-1} - k\mathbf{v}^m, \psi_s)_{\mathcal{S}^m} + k((\mathbf{v}^m - \partial_t T_m)\nabla\mathbf{u}^m, \psi_s)_{\mathcal{S}^m} = 0,\\ (\mathrm{div}\ \mathbf{v}^m, \xi_f)_{\mathcal{F}(t)} + S(p^m, \xi_f) = 0\end{aligned}$$

for all $\phi \in \mathcal{V}^m$, $\psi_s \in \mathcal{W}_s^m$ and for all $\xi_f \in \mathcal{L}_f^m$.

The only quantity related to the transformation to be calculated is $\partial_t T$. Therefore, we first compute the point $x^{m-1} = T_m(x^m, t_{m-1})$ by (12.4). Now, differentiating (12.3) yields

$$\partial_t T(x^m, t_m) = \frac{x^m - x^{m-1}}{t_m - t_{m-1}}.$$

With this time stepping scheme, we can get arbitrarily close to contact. Real contact is not possible, however, as this would destroy the local regularity of the mapping T_m. To cope with this, we modify the scheme in the contact region when the ball comes close to the ground by choosing $T_m = \mathrm{id}$ there.

12.4 Stabilization of the Solid Equations

The full fluid-structure interaction problem (12.1) contains a regularity problem at the interface $\mathcal{I}(t)$, as described in Sect. 3.1.4. The natural trial space for the solid velocity in the variational formulation is $L^2(\mathcal{S}(t))^2$, which means that a trace on the interface $\mathcal{I}(t)$ is not well-defined. The trace is however needed for the *kinematic* interface condition $\mathbf{v}_f = \partial_t \mathbf{u}_s$ on $\mathcal{I}(t)$. Furthermore, numerical tests show that the solid velocity is sensitive to stability problems caused by perturbations or discretization errors, especially in the interface region (see Chap. 4 in [151]).

To analyze this problem, we will first of all focus on the simplest form of a solid equation, a linear wave equation on a fixed domain $\mathcal{S}$, and study different techniques

to handle the aforementioned problems. In mixed variational formulation, the system of equations is given by: *Find* $\mathbf{u} \in \mathcal{W}, \mathbf{v} \in \mathcal{V}$ *such that*

$$\begin{aligned} (\partial_t \mathbf{v}, \phi)_{\mathcal{S}} + \lambda(\nabla \mathbf{u}, \nabla \phi)_{\mathcal{S}} = 0 \quad \forall \phi \in \mathcal{W}, \\ (\partial_t \mathbf{u}, \psi)_{\mathcal{S}} - (\mathbf{v}, \psi)_{\mathcal{S}} = 0 \quad \forall \psi \in \mathcal{V}, \end{aligned} \tag{12.5}$$

with a positive parameter $\lambda > 0$. Testing with $\phi = \partial_t \mathbf{u}$ and $\psi = \partial_t \mathbf{v}$ and integrating by parts in time, we see that the homogeneous wave equation is energy-conserving in the following sense for $t > 0$

$$\lambda \|\nabla \mathbf{u}(t)\|_{\mathcal{S}}^2 + \|\mathbf{v}(t)\|_{\mathcal{S}}^2 = \lambda \|\nabla \mathbf{u}(0)\|_{\mathcal{S}}^2 + \|\mathbf{v}(0)\|_{\mathcal{S}}^2. \tag{12.6}$$

Hence, any kind of perturbations will not be damped, but it is conserved and may accumulate over time. Furthermore, (12.6) gives neither control over derivatives of $\mathbf{v}$ nor over the trace of $\mathbf{v}$ on the boundary of $\mathcal{S}$.

To increase the stability, we use a simple, stabilization technique: *Find* $\mathbf{u}_h \in \mathcal{W}_h, \mathbf{v}_h \in \mathcal{V}_h$ *such that*

$$\begin{aligned} (\partial_t \mathbf{v}_h, \phi_h)_{\mathcal{S}} + \lambda(\nabla \mathbf{u}_h, \nabla \phi_h)_{\mathcal{S}} = 0 \quad \forall \phi_h \in \mathcal{W}_h, \\ (\partial_t \mathbf{u}_h, \psi_h)_{\mathcal{S}} - (\mathbf{v}_h, \psi_h)_{\mathcal{S}} - \alpha h^s (\nabla \mathbf{v}_h, \nabla \psi_h)_{\mathcal{S}} = 0 \quad \forall \psi_h \in \mathcal{V}_h. \end{aligned} \tag{12.7}$$

The exponent s is typically chosen in the interval $s \in [1, 2]$, see [151]. For this formulation, the energy conservation reads

$$\begin{aligned} \lambda \|\nabla \mathbf{u}_h(t)\|_{\mathcal{S}}^2 + \|\mathbf{v}_h(t)\|_{\mathcal{S}}^2 + \alpha h^s \|\nabla \mathbf{v}_h(t)\|_{\mathcal{S}}^2 \\ = \lambda \|\nabla \mathbf{u}_h(0)\|_{\mathcal{S}}^2 + \|\mathbf{v}_h(0)\|_{\mathcal{S}}^2 + \alpha h^s \|\nabla \mathbf{v}_h(0)\|_{\mathcal{S}}^2. \end{aligned} \tag{12.8}$$

We conclude that this formulation gives us control over the derivatives of $\mathbf{v}_h$ and thus (by the trace lemma) over the trace of the velocity on $\partial\mathcal{S}$.

To further motivate, why this formulation increases stability, we consider a standard time discretization with the backward Euler method and multiply the second equation by -1. Problem (12.7) reads in matrix form

$$\begin{pmatrix} \lambda A_h & \frac{1}{k} M_h \\ -\frac{1}{k} M_h & M_h + \alpha h^s A_h \end{pmatrix} \begin{pmatrix} \mathbf{u}_h^{m+1} \\ \mathbf{v}_h^{m+1} \end{pmatrix} = \begin{pmatrix} \frac{1}{k} \mathbf{v}_h^m \\ -\frac{1}{k} \mathbf{u}_h^m \end{pmatrix}, \tag{12.9}$$

where M_h is the discrete mass matrix and A_h the discrete Laplacian. We see that the stabilization term increases the diagonal part of the matrix significantly, especially for $s \leq 2$. It can be interpreted as adding artificial diffusion to the diagonal part of the system matrix. For the derivation of a priori error estimates depending on s for the stabilized, discrete formulation, we refer to [151, 152].

12.5 Treatment of Contact

In the cases where no fluid layer remains between the ball and the ground, we have to apply a contact algorithm to simulate the bounce-off of the ball. A simple contact algorithm has been used by Sathe and Tezduyar [298]. The idea is to add an artificial contact force g_c on the interface to the balance of momentum if the ball comes very close to the ground. The force depends on the distance to the ground and goes to infinity as the distance tends to zero. Hence, contact becomes in principle impossible. In this way, the modeling issues connected to the Navier-Stokes equations and contact that were mentioned at the beginning of this chapter are to a certain degree circumvented. We will see below, however, that numerical contact might still happen, at least unless the time step size is chosen sufficiently small.

The modified interface condition reads

$$(\boldsymbol{\sigma}_f - g_c I)\mathbf{n}_f = \boldsymbol{\sigma}_s \mathbf{n}_f,$$

where the contact force is defined by

$$g_c(x) = \begin{cases} 0 & \operatorname{dist}(x, \Gamma_w) \geq \operatorname{dist}_0, \\ \gamma_c \frac{\operatorname{dist}(x,\Gamma_w) - \operatorname{dist}_0}{\operatorname{dist}(x,\Gamma_w)} & \operatorname{dist}(x, \Gamma_w) < \operatorname{dist}_0, \end{cases}$$

on $\mathcal{I}$ with a contact parameter γ_c and a reference distance dist_0.

More involved contact strategies are based on variational inequalities (see e.g. Diniz dos Santos et al. [122], Mayer et al. [237], Pironneau [259]) imposing the constraint

$$\operatorname{dist}(x, \Gamma_w) \geq 0 \quad \text{on } \mathcal{I}.$$

To ensure the well-posedness of the system of equations, a Lagrange multiplier is added to the balance of momentum that acts similar to the contact force g_c when the constraint is active. Due to the additional computational complexity of numerical algorithms for variational inequalities, we stick here to the prior simple contact algorithm. For further studies we refer to the literature [155].

12.6 Numerical Examples

12.6.1 Example 1: Configuration Without Contact

For the first test, we use the Lamé parameters $\mu_s = 2 \cdot 10^5 \,\mathrm{kg} \cdot \mathrm{m}^{-1}\mathrm{s}^{-2}$ and $\lambda_s = 8 \cdot 10^5 \,\mathrm{kg} \cdot \mathrm{m}^{-1}\mathrm{s}^{-2}$ and the fluid viscosity $\nu_f = 10^{-3} \,\mathrm{m}^2 \cdot \mathrm{s}^{-1}$. The fluid and solid density are $\rho_s = \rho_f = 10^3 \,\mathrm{kg} \cdot \mathrm{m}^{-3}$. In this example, we do not apply the

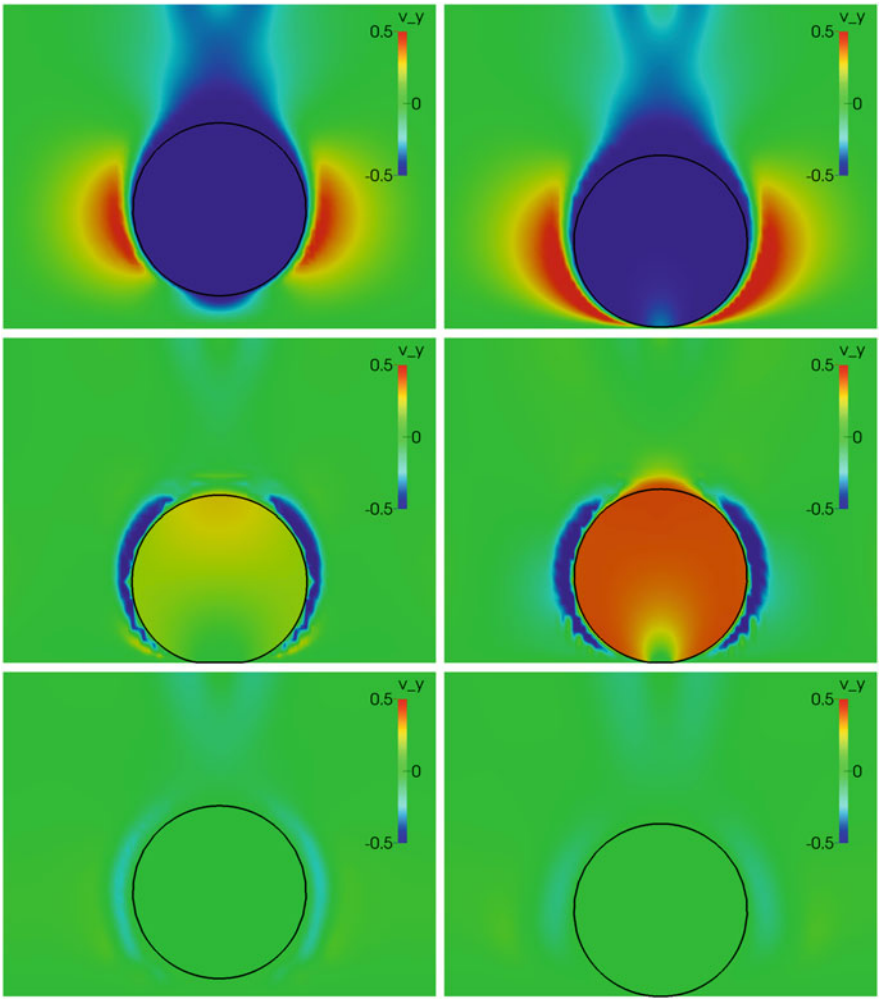

Fig. 12.3 Illustration of the free fall of an elastic ball, its contact with the ground and the subsequent rebound at six different times. The color illustrates the vertical velocity $\mathbf{v}_y$ and the *black contour line* is the discrete interface

contact force introduced in Sect. 12.5, as it turns out that for this specific choice of parameters, a small fluid layer remains between ball and bottom anyway.

In Fig. 12.3, we show the falling ball at six different instances of time. First, the ball is accelerated by gravity and falls down. At time $t \approx 1.6\,\mathrm{s}$, the bottom is almost reached and the ball slows down due to a high fluid pressure. It comes closest to the ground at time $t \approx 1.8\,\mathrm{s}$, where the minimal distance is $d \approx 1.2 \cdot 10^{-3}\,\mathrm{m}$. At this time the ball is significantly compressed at its bottom.

The discretization at this point is illustrated in Fig. 12.4 (top) for the coarsest mesh we used. The interface shows a domed shape due to a high fluid pressure in the middle (see Fig. 12.5) and the minimal distance is not attained in the center but left and right of it. In this configuration, there is no real contact but a small layer of fluid remains between ball and ground. Nevertheless, here and in the following we will call this period the "contact time" or "contact interval" for simplicity.

Then, due to the compression at the bottom the ball is accelerated upwards. The ball reaches its highest elevation at a maximum distance $d \approx 8.3 \cdot 10^{-2}$ m from the ground at time $t \approx 2.4$ s and falls down again. After a smaller second bounce with distance $d \approx 4.6 \cdot 10^{-3}$ m, it comes to rest, being in real contact with the ground at

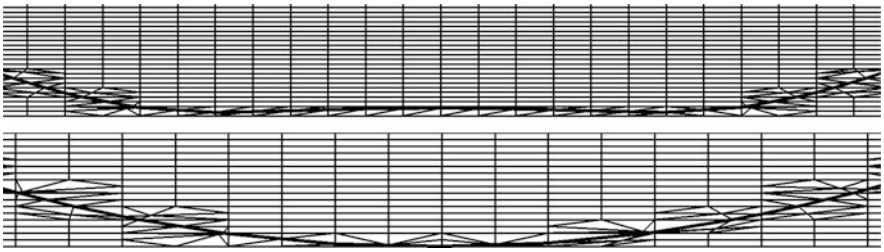

Fig. 12.4 Illustration of a coarse mesh during the first rebound (*top sketch*) and at the end time when the ball is at rest (*lower sketch*). During the first rebound, a small layer of fluid remains between ball and ground

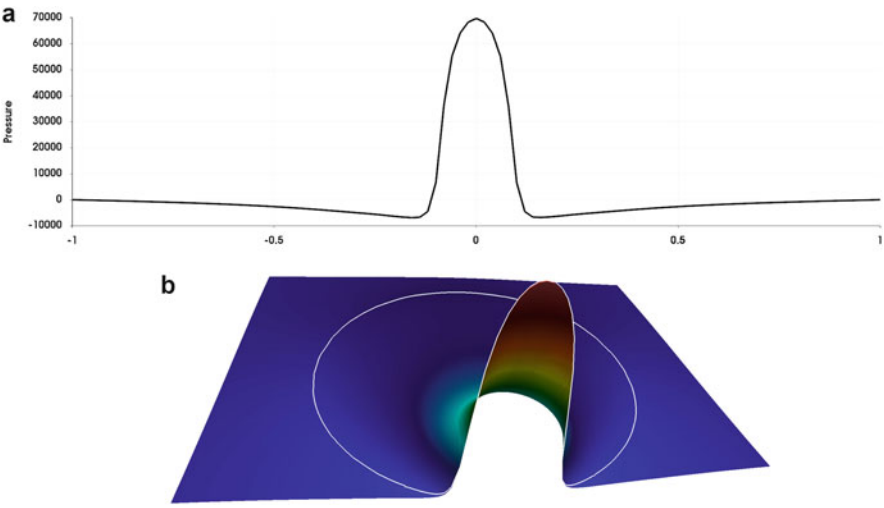

Fig. 12.5 Pressure peak during the contact between ball and ground. (**a**) Pressure value along the boundary line $\Gamma_w = \{(x, -1),\ 0 < x < 1\}$. (**b**) Pressure close to contact. Inside the ball we show the harmonic extension of the pressure (without a physical connotation). The *white contour line* shows the boundary of the elastic ball

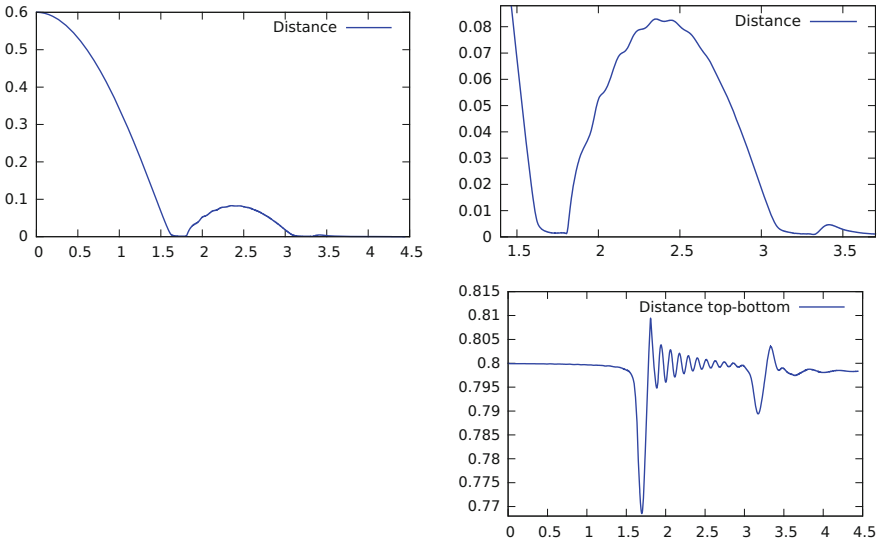

Fig. 12.6 Distance of the ball from the bottom and width of the ball. *Top:* Minimal distance between ball and ground over time and a zoom-in at the interval of contact and rebound. *Right:* Size of the ball (distance between *top and bottom*)

time $t \approx 4.4\,\mathrm{s}$, see Fig. 12.4 (bottom) for an illustration of the mesh at the time of real contact.

In Fig. 12.6, we plot the minimal distance between the ball and the ground including a zoom-in of the contact and rebound interval in the upper row. Furthermore, we show the distance between the top and the bottom of the ball and an averaged vertical velocity of the solid in the lower row.

In the lower left plot, we observe that the distance between the top and the bottom of the ball attains minima at the two contact times due to the compression. After the rebounds, we observe oscillations that get smaller over time. These oscillations are physical: First, the ball is maximally compressed at the bottom at the contact time. Once the ball bounces off again, the deformation is relaxed. The ball is even overstretched at some point and starts to oscillate between an expanded and a compressed state periodically.

12.6.2 Convergence Studies

We study the test configuration on different grids and for different time step sizes. The finite element meshes, we use are highly refined in the contact region. The coarsest mesh consists of patches of size of size $2.5 \cdot 10^{-2}\,\mathrm{m} \times 3.1 \cdot 10^{-3}\,\mathrm{m}$ in the contact region and $0.1\,\mathrm{m} \times 0.15\,\mathrm{m}$ in the upper right and upper left part. Furthermore,

Table 12.1 *Top:* Minimal distance between ball and ground during the first contact interval and maximal distance after the first rebound

	First contact: minimum distance			First bounce: maximum distance		
#nodes \ k	$2 \cdot 10^{-3}$	$1 \cdot 10^{-3}$	$5 \cdot 10^{-4}$	$2 \cdot 10^{-3}$	$1 \cdot 10^{-3}$	$5 \cdot 10^{-4}$
4225	$6.38 \cdot 10^{-4}$	$6.49 \cdot 10^{-4}$	$6.26 \cdot 10^{-4}$	$4.71 \cdot 10^{-2}$	$5.19 \cdot 10^{-2}$	$5.20 \cdot 10^{-2}$
16641	$1.22 \cdot 10^{-3}$	$1.24 \cdot 10^{-3}$	$1.24 \cdot 10^{-3}$	$7.41 \cdot 10^{-2}$	$8.29 \cdot 10^{-2}$	$8.49 \cdot 10^{-2}$
66049	–	$1.27 \cdot 10^{-3}$	$1.27 \cdot 10^{-3}$	–	$8.71 \cdot 10^{-2}$	$8.96 \cdot 10^{-2}$

	Relative mass conservation error		
#nodes \ k	$2 \cdot 10^{-3}$	$1 \cdot 10^{-3}$	$5 \cdot 10^{-4}$
4225	$8.96 \cdot 10^{-3}$	$8.94 \cdot 10^{-3}$	$8.94 \cdot 10^{-3}$
16641	$2.54 \cdot 10^{-3}$	$2.36 \cdot 10^{-3}$	$2.31 \cdot 10^{-3}$
66049	–	$5.07 \cdot 10^{-4}$	$5.05 \cdot 10^{-4}$

Bottom: Relative error in mass conservation at time $t = 3$ s. The three functionals are calculated for three different time step sizes and on three different meshes

we show the results on two finer meshes that are obtained from this coarse mesh by global refinement.

In the upper part of Table 12.1, we show the minimal distance during the first contact and the maximum elevation after the first rebound and the error in mass conservation on these meshes for three different time step sizes. We observe that both the minimal distance during the contact and the maximal distance after the rebound are significantly smaller on the coarsest mesh. On the other hand, the results on the finer meshes show good agreement. While on the finest mesh, the minimum distance, i.e. the minimum height of the fluid layer, is a little less then two patches, on the coarsest patch only about a quarter of a patch remains on the fluid side at the narrowest point. We conclude that the resolution of the contact region on the coarse mesh was not fine enough to resolve the contact dynamics appropriately.

In the lower part of Table 12.1, we show the relative error in mass conservation is defined by

$$j_{\text{mass}} = \left| \frac{\pi r^2 \rho_s^0 - \int_S J \rho_s^0 \, \mathrm{dx}}{\pi r^2 \rho_s^0} \right|$$

for different spatial and temporal discretization parameters. We observe a good convergence behavior in both space and time, even on the coarsest mesh. The spatial discretization error is dominating and decreases with order $\mathcal{O}(h_P^2)$. This convergence behavior was expected, as it is the approximation error of the interface, see Sect. 4.5. Furthermore, this result indicates that the Eulerian approach in combination with the described discretization techniques, shows very good mass conservation properties.

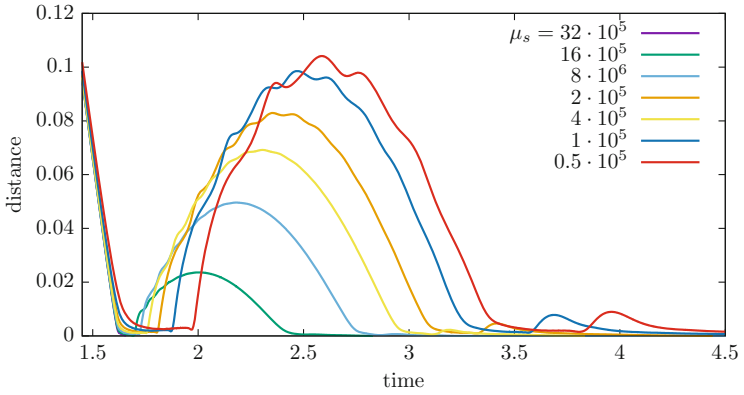

Fig. 12.7 Distance between ball and ground over time for different solid parameters μ_s during the contact and rebound interval. The first Lamé parameter is chosen as $\lambda_s = 4\mu_s$. The rebound height is higher for softer solids

12.6.3 Influence of Material Parameters

Next, we want to address the question of whether a small layer of fluid is maintained between ball also for different parameters. Therefore, we increase and decrease the solid Lamé parameters, keeping the ratio between the Lamé parameters μ_s and λ_s constant, $\lambda_s = 4\mu_s$ (which corresponds to a Poisson ration of $\nu_s = 0.4$).

For a set of parameters ranging from $\mu_s = 5 \cdot 10^4\,\mathrm{kg \cdot m^{-1}s^{-2}}$ to $3.2 \cdot 10^6\,\mathrm{kg \cdot m^{-1}s^{-2}}$, we plot the distances between ball and ground over time in Fig. 12.7. For the stiffest material ($\mu_s = 3.2 \cdot 10^6\,\mathrm{kg \cdot m^{-1}s^{-2}}$) no fluid layer remains during the first contact interval. Ball and ground are in real contact. Once the ball is in contact with the ground, the *no-slip* condition on Γ_w used here, prevents it from bouncing. The same happens for the second stiffest material ($\mu_s = 1.6 \cdot 10^6\,\mathrm{kg \cdot m^{-1}s^{-2}}$) at the second contact time. It is, however, questionable, whether this corresponds to the physical situation. Instead, the contact might be caused by numerical errors due to a too large time step or an insufficient grid resolution in the contact region. We will use the configuration with the largest Lamé parameters below to study the proposed contact algorithm.

For the remaining parameters, the solid bounces twice. Due to a higher compression during the contact, the first and the second rebound heights are bigger, the softer the solid is.

12.6.4 Contact Algorithm

As the simple contact algorithm used is not physically motivated, but is based on an artificial force g_d, we have to analyze its effect on the contact dynamics. Therefore,

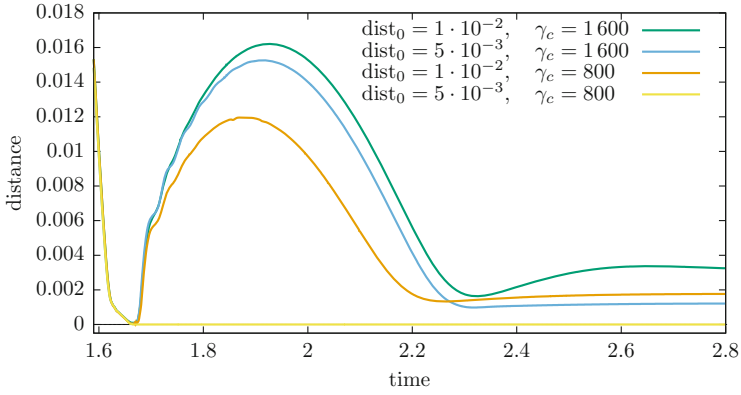

Fig. 12.8 Influence of different contact parameters γ_c and dist_0 for the Lamé parameters $\mu_s = 3.2 \cdot 10^6\,\text{kg} \cdot \text{m}^{-1}\text{s}^{-2}$, $\lambda_s = 1.28 \cdot 10^7\,\text{kg} \cdot \text{m}^{-1}\text{s}^{-2}$. The contact force with parameters $\gamma_c = 800$ and $\text{dist}_0 = 5 \cdot 10^{-3}$ m as well as for $\gamma_c \leq 400$ or $\text{dist}_0 \leq 10^{-3}$ m was not large enough to prevent the contact

we consider the situation from above with the stiffest material parameters $\mu_s = 3.2 \cdot 10^6\,\text{kg} \cdot \text{m}^{-1}\text{s}^{-2}$ and $\lambda_s = 1.28 \cdot 10^7\,\text{kg} \cdot \text{m}^{-1}\text{s}^{-2}$ where a contact algorithm is necessary. We use $\text{dist}_0 = 10^{-3}$ m, $5 \cdot 10^{-3}$ m and 10^{-2} m and the contact parameters $\gamma_c = 800$ and 1600.

For the smallest contact distance $\text{dist}_0 = 10^{-3}$ m, contact could not be prevented with the chosen time step and grid size. The same occurred for $\text{dist}_0 = 5 \cdot 10^{-3}$ m and the smaller parameter $\gamma_c = 800$. We plot the distances to the ground over time in Fig. 12.8 for the calculations with $\text{dist}_0 \geq 5 \cdot 10^{-3}$ m. The plot shows significant differences. For example, for the largest parameters $\text{dist}_0 = 10^{-2}$ m and $\gamma_c = 1600$, the rebound height is 35% bigger than for the same reference distance with $\gamma_c = 800$.

Furthermore, the ball stays at rest at a distance of $3.18 \cdot 10^{-3}$ m from the ground which is rather large compared to $\text{d}_{\text{rest}} \approx 1.77 \cdot 10^{-3}$ m for $\gamma_c = 800$ and $\text{d}_{\text{rest}} \approx 1.21 \cdot 10^{-3}$ m for $\text{dist}_0 = 5 \cdot 10^{-3}$ m. Here it is obvious that this distance depends more on the artificial contact force than on physical effects.

We conclude that the contact parameters have to be chosen carefully and their influence must be taken into account when interpreting the results. The investigation of more sophisticated contact algorithms is subject to ongoing research.

12.6.5 Example 2: Bouncing Down the Stairs

Finally, we will study a more complex numerical example, i.e. an elastic ball bouncing down some stairs. We give a sketch of the geometry under consideration in Fig. 12.9. In order to get the desired direction, we let the ball bounce on an inclined

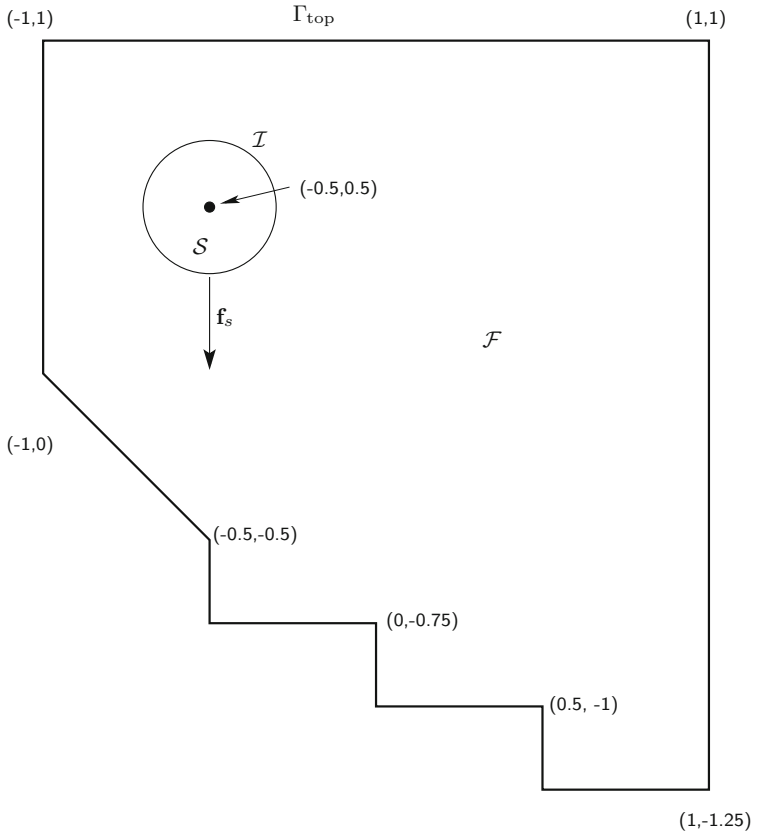

Fig. 12.9 Sketch of the configuration of the second example and the initial mesh. To simulate the contact dynamics accurately, fine mesh cells are used in the contact regions

plane first. Afterwards, it bounces down three stairs. Depending on the material parameters it can bounce once or several times on a stair or just roll over it. We consider the lower, left and right walls as rigid and impose a homogeneous Dirichlet condition for the velocity there. On the top Γ_{top}, we use again a *do-nothing* boundary condition. We use the same material parameters as in Sect. 12.6.1 and vary only the fluid density to $\rho_f = 100\,\text{kg}\cdot\text{m}^{-3}$, $150\,\text{kg}\cdot\text{m}^{-3}$, $300\,\text{kg}\cdot\text{m}^{-3}$ and $1000\,\text{kg}\cdot\text{m}^{-3}$.

We show snapshots of the horizontal velocity at twelve different times in Fig. 12.10 for $\rho_f = 300\,\text{kg}\cdot\text{m}^{-3}$. The ball drops onto the inclined plane and bounces to the right. The next contact is on the right part of the first stair. Afterwards, we observe three bounces on the second stair and two on the third one, before the ball comes to rest.

In Fig. 12.11, we show contours of the ball for calculations with $\rho_f = 100\,\text{kg}\cdot\text{m}^{-3}$, $150\,\text{kg}\cdot\text{m}^{-3}$, $300\,\text{kg}\cdot\text{m}^{-3}$ and $1000\,\text{kg}\cdot\text{m}^{-3}$. For the two larger density values, we use a contact force with parameters $\gamma_c = 5\cdot 10^3$ and

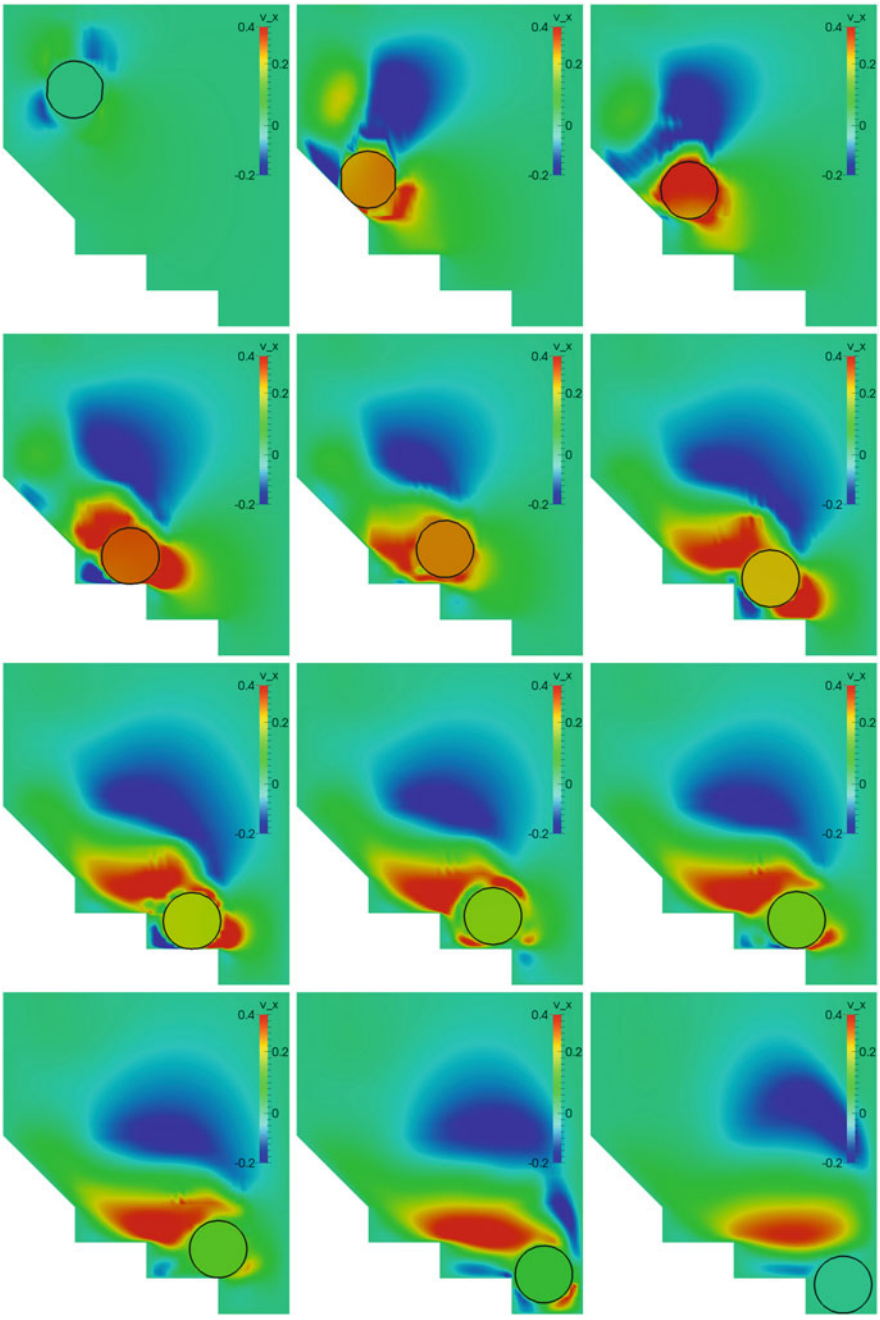

Fig. 12.10 Ball bouncing down three stairs for $\rho_f = 300\,\mathrm{kg}\cdot\mathrm{m}^{-3}$ at twelve different times. The *color* illustrates the horizontal velocity $\mathbf{v}_x$, the *black contour line* is the discrete interface. *First row:* Free fall, contact with the inclined plane and rebound. *Second row:* Contact with the first stair and rebound. *Third row:* First contact with the second stair, small bounce and second contact. *Last row:* Third contact with the second stair, fall and position at rest

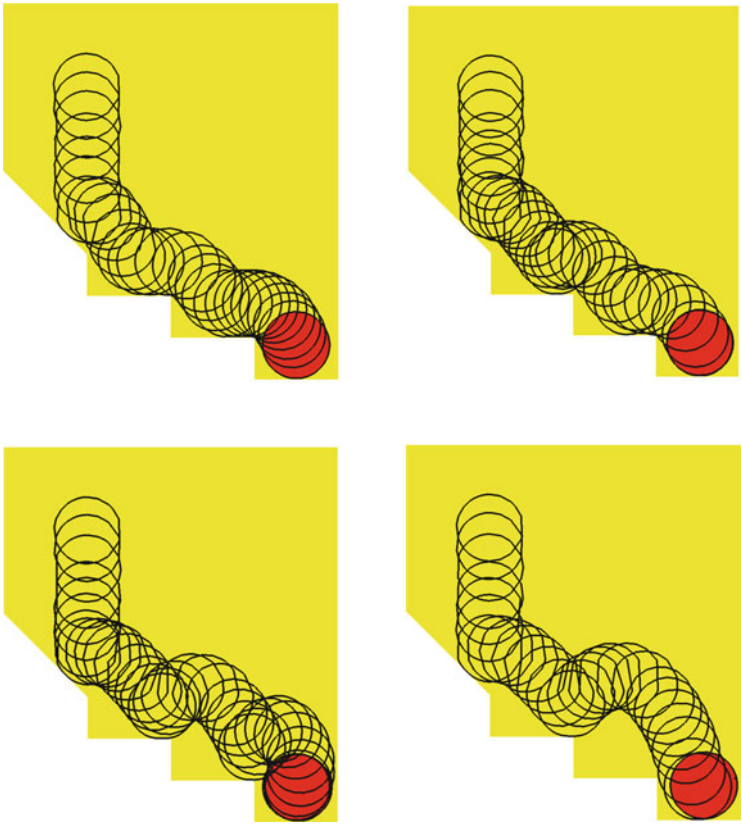

Fig. 12.11 Contour plots of the interface at several times. *Top left:* $\rho_f = 1000\,\mathrm{kg}\cdot\mathrm{m}^{-3}$, *top right:* $\rho_f = 300\,\mathrm{kg}\cdot\mathrm{m}^{-3}$, *bottom left:* $\rho_f = 150\,\mathrm{kg}\cdot\mathrm{m}^{-3}$, *bottom right:* $\rho_f = 100$. While for $\rho_f = 1000\,\mathrm{kg}\cdot\mathrm{m}^{-3}$ the ball rolls over the stairs, the ball bounces exactly once on each stair for $\rho_f = 150\,\mathrm{kg}\cdot\mathrm{m}^{-3}$. For $\rho_f = 100\,\mathrm{kg}\cdot\mathrm{m}^{-3}$, the ball jumps and skips the second stair

$\mathrm{dist}_0 = 10^{-2}\,\mathrm{m}$. For $\rho_f \leq 150\,\mathrm{kg}\cdot\mathrm{m}^{-3}$ this force was not large enough to prevent the contact (see the contact parameter studies below). Here, we use $\gamma_c = 10^4$.

The rebounds are higher, the smaller the fluid density is. For $\rho_f = 100\,\mathrm{kg}\cdot\mathrm{m}^{-3}$ the rebound at the first stair is so high that the ball jumps over the second stair and has its next contact on the third one. On the third stair we obtain six small bounces before the ball comes to rest.

For $\rho_f = 150\,\mathrm{kg}\cdot\mathrm{m}^{-3}$, the ball bounces exactly once on the first and second stair. Before dropping onto the last stair, the ball gets quite close to the right wall with a minimal distance of approximately $2\cdot 10^{-2}\,\mathrm{m}$. However, it is slowed down by fluid forces before the contact force corresponding to the right wall would get active. For $\rho_f = 300\,\mathrm{kg}\cdot\mathrm{m}^{-3}$, the rebounds are already significantly smaller and for $\rho_f = 1000\,\mathrm{kg}\cdot\mathrm{m}^{-3}$, the ball bounces once on each stair and continues rolling to the right.

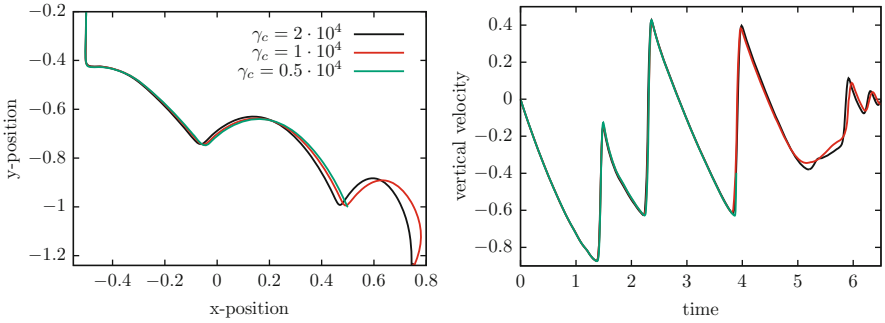

Fig. 12.12 *Left:* Position of the bottom of the ball. *Right:* Averaged vertical velocity over time for $\rho_f = 150\,\mathrm{kg} \cdot \mathrm{m}^{-3}$ and different values of the contact force. For $\gamma_c = 5 \cdot 10^3$ the contact could not be prevented at the contact time with the second stair

Finally, we study the influence of the contact force. In Fig. 12.12 (left sketch), we plot the trajectories of the lower bottom of the ball for $\rho_f = 150\,\mathrm{kg} \cdot \mathrm{m}^{-3}$ and three different contact force parameters γ_c. On the right, we plot an averaged vertical velocity $\overline{\mathbf{v}}_y$ over time.

The contact force with parameter $\gamma_c = 5 \cdot 10^3$ prevents the contact on the inclined plane and on the first stair, but it fails on the second one. Moreover, we observe that for larger contact parameters the velocity of the ball is slightly higher, and the ball bounces earlier on each stair. As a consequence, the ball almost touches the right wall for $\gamma_c = 10^4$ when it falls down towards the third stair, while it remains at a significantly larger distance of around $6 \cdot 10^{-2}\,\mathrm{m}$ for $\gamma_c = 2 \cdot 10^4$. The averaged velocities show good agreement before the bounce on the second stair and differ slightly afterwards due to the different trajectories.

We conclude that in this final example the influence of the contact force was relatively small. However, some quantities of interest, e.g. the contact distance (if there is any) or the distance at rest, cannot be determined with this approach and require more sophisticated contact algorithms.